A new divergence method to quantify methane emissions using observations of Sentinel-5P TROPOMI

Mengyao Liu[1], Mengyao Liu[1], Ronald Van Der A[1], Michiel Van Weele[1], Henk Eskes[1], Xiao Lu[2], Pepijn Veefkind[1], Jos De Laat[1], Hao Kong[3], Jinxu Wang[4], Jiyunting Sun[1], Jieying Ding[1], Yuanhong Zhao[4], and Hongjian Weng[3]

[1]KNMI
[2]Harvard University
[3]Peking University
[4]Ocean University of China

November 22, 2022

Abstract

Key points: * A new divergence method is developed to estimate methane emissions based on satellite observations, requiring no a priori emissions. * The applicability of this method in identifying and quantifying sources is proven by a GEOS-Chem simulation with known a priori emissions. * The estimated emissions over Texas (United States) based on TROPOMI observations are evaluated and are found to be robust. Abstract We present a new divergence method to estimated methane (CH 4) emissions from satellite observed mean mixing ratio of methane (XCH 4) by deriving the regional enhancement of XCH 4 in the Planetary Boundary Layer (PBL). The applicability is proven by comparing the estimated emissions with its a priori emission inventory from a 3-month GEOS-Chem simulation. When applied to TROPOspheric Monitoring Instrument (TROPOMI) observations, sources from well-known oil/gas production areas, livestock farms and wetlands in Texas become clearly visible in the emission maps. The calculated yearly averaged total CH 4 emission over the Permian Basin is 3.06 [2.82, 3.78] Tg a-1 for 2019, which is consistent with previous studies and double that of EDGAR v4.3.2 for 2012. Sensitivity tests on PBL heights, on the derived regional background and on wind speeds suggest our divergence method is quite robust. It is also a fast and simple method to estimate the CH 4 emissions globally. Plain Language Summary Methane (CH 4) is an important greenhouse gas in the atmosphere and plays a crucial role in the global climate change. It kept increasing over the last decades. About 70% of CH 4 comes from human activities like oil/gas productions or livestock farms. The recently launched TROPOspheric Monitoring Instrument (TROPOMI) provides an opportunity to estimate the emissions of CH 4 on a regional scale. This work presents a new method to fastly derive CH 4 emissions at a fairly high spatial resolution without a priori knowledge of sources.

A new divergence method to quantify methane emissions using observations of Sentinel-5P TROPOMI

Mengyao Liu[1]*, Ronald van der A[1,2], Michiel van Weele[1], Henk Eskes[1], Xiao Lu[3], Pepijn Veefkind[1, 4], Jos de Laat[1], Hao Kong[5], Jinxu Wang[6], Jiyunting Sun[1], Jieying Ding[1], Yuanhong Zhao[6], Hongjian Weng[5]

[1] KNMI, Royal Netherlands Meteorological Institute, De Bilt, The Netherlands

[2] Nanjing University of Information Science & Technology (NUIST), Nanjing, China

[3] School of Engineering and Applied Sciences, Harvard University, Cambridge, MA 02138, USA

[4] Delft University of Technology, Delft, The Netherlands

[5] Department of Atmospheric and Oceanic Sciences, School of Physics, Peking University, Beijing, China

[6] College of Oceanic and Atmospheric Sciences, Ocean University of China, Qingdao, China

* Correspondence to: Mengyao Liu (mengyao.liu@knmi.nl)

Key points:

- A new divergence method is developed to estimate methane emissions based on satellite observations, requiring no a priori emissions.
- The applicability of this method in identifying and quantifying sources is proven by a GEOS-Chem simulation with known a priori emissions.
- The estimated emissions over Texas (United States) based on TROPOMI observations are evaluated and are found to be robust.

Abstract

We present a new divergence method to estimated methane (CH_4) emissions from satellite observed mean mixing ratio of methane (XCH_4) by deriving the regional

enhancement of XCH_4 in the Planetary Boundary Layer (PBL). The applicability is proven by comparing the estimated emissions with its a priori emission inventory from a 3-month GEOS-Chem simulation. When applied to TROPOspheric Monitoring Instrument (TROPOMI) observations, sources from well-known oil/gas production areas, livestock farms and wetlands in Texas become clearly visible in the emission maps. The calculated yearly averaged total CH_4 emission over the Permian Basin is 3.06 [2.82, 3.78] Tg a^{-1} for 2019, which is consistent with previous studies and double that of EDGAR v4.3.2 for 2012. Sensitivity tests on PBL heights, on the derived regional background and on wind speeds suggest our divergence method is quite robust. It is also a fast and simple method to estimate the CH_4 emissions globally.

Plain Language Summary

Methane (CH_4) is an important greenhouse gas in the atmosphere and plays a crucial role in the global climate change. It kept increasing over the last decades. About 70% of CH_4 comes from human activities like oil/gas productions or livestock farms. The recently launched TROPOspheric Monitoring Instrument (TROPOMI) provides an opportunity to estimate the emissions of CH_4 on a regional scale. This work presents a new method to fastly derive CH_4 emissions at a fairly high spatial resolution without a priori knowledge of sources.

1 Introduction

Methane (CH_4) is the second most important anthropogenic greenhouse gas after carbon dioxide (CO_2) and is also a principal precursor of tropospheric ozone [*Shindell et al.*, 2012]. In-situ measurements show a continuous increase of methane over the last decades [*Dlugokencky et al.*, 2009; *IPCC*, 2013; *Saunois et al.*, 2016; *Turner et al.*, 2019], with stable concentrations from 2000 to 2006 [*Dlugokencky et al.*, 2009; *Rigby et al.*, 2008]. CH_4 has both natural (e.g., wetlands, wildfires, termites) and anthropogenic (e.g., fossil fuels, livestock, landfills and wastewater treatments) sources. About 360 million tons (60 % of the total CH_4) are released through human activities [*Saunois et al.*, 2020]. The relatively short lifetime of CH_4 (about a decade) makes it a short-term target for mitigating climate change by reducing the emissions.

Satellite observations of CH_4 provide an efficient way to analysis its variations and emissions at a regional to global scale [*Buchwitz et al.*, 2017; *Lunt et al.*, 2019; *J. D. Maasakkers et al.*, 2019; *Miller et al.*, 2019; *Zhang et al.*, 2020]. Compared to previous widely used instruments like Greenhouse gases Observing SATellite (GOSAT) and SCanning Imaging Absorption spectroMeter for Atmospheric CartograpHY (SCIAMACHY, onboard Envisat), the TROPOspheric Monitoring Instrument

(TROPOMI) on board the Sentinel 5 Precursor (S5-P) satellite measures CH_4 at an unprecedented resolution of $7 \times 7\ km^2$ since its launch in October 2017 (upgraded to $5.5 \times 7\ km^2$ in August 2019) [*Veefkind et al.*, 2012]. Several studies have shown the capability of TROPOMI on identifying and quantifying the sources at a local to regional scale (e.g., [*de Gouw et al.*, 2020; *Pandey et al.*, 2019; *Schneider et al.*, 2020; *Zhang et al.*, 2020]). These studies mainly focused on oil/gas leakage events, which show strong signals that can be easily identified, or they are using an inverse modeling relying on an a-priori emission inventory.

Freshly emitted air pollutants are usually concentrated around the emission source, in the case of not too high wind speeds [*Liu et al.*, 2020]. *Beirle et al.* [2019] found that the strong gradients near sources of nitrogen oxides (NO_x) are preserved by averaging horizontal fluxes. Therefore, the divergence of horizontal fluxes of nitrogen dioxide (NO_2) plus a sink term can be used to estimate the emissions of NO_2. In our study, we apply a divergence method for deriving CH_4 emissions. The sink term can be ignored for CH_4 because of its relatively long lifetime, which makes it more straightforward to link the divergence to the emission. The divergence works on the product of horizontal fluxes and wind fields, which is independent of a priori emission inventories and models and can be applied at various resolutions regionally or globally.

The retrieved CH_4 from satellite observations are the ratios of methane total vertical columns to air density columns (XCH_4), which are strongly affected by the stratospheric abundance. Thus the influence of transportation in the upper atmosphere and of orography should be removed to better distinguish gradients due to emissions. XCH_4 measured by satellites reflects the abundance of the background plus the newly emitted methane because of its around 10-year lifetime. Hence the contribution from the background should be deducted when estimating the emissions.

In this study, we present a new divergence method to quantify the emission of CH_4 from satellite retrieved XCH_4. The XCH_4 of TROPOMI is first destriped and corrected with albedos at short-wave infrared (SWIR) wavelengths (2305–2385 nm) to improve the data quality. Before applying the method to TROPOMI observations, a 3-month (from July 2012 to September 2012) hourly GEOS-Chem nested model simulation over North America is used to test the applicability of our method. The data quality of the resulting emissions is further analyzed with sensitivity studies and comparisons to the literature.

2 Method and Data

Figure 1 shows the flowchart of the procedure to estimate the CH_4 emissions from TROPOMI retrieved XCH_4. It consists of three main steps. First, applying posteriori corrections on XCH_4 to reduce the systematic biases caused by across-track biases and surface albedos. Second, the mean mixing ratios of CH_4 in the PBL (XCH_4^{PBL}) and the corresponding regional backgrounds are derived by subtracting the columns above the

PBL, which are estimated by XCH_4 profiles from the Atmospheric Composition Reanalysis 4 (EAC4) of the Copernicus Atmosphere Monitoring Service (CAMS) [*Inness et al.*, 2019]. The enhancements of XCH_4^{PBL} are further used to calculate the spatial divergence and estimate CH_4 emissions.

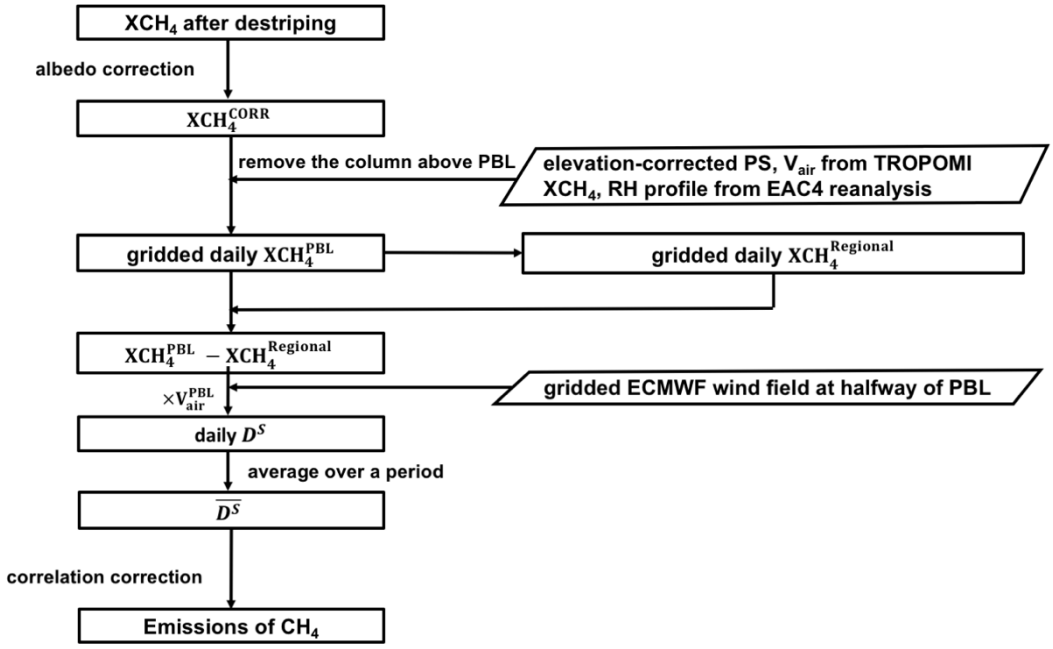

Figure 1. The flow chart of using TROPOMI XCH_4 to derive the CH_4 emissions over a certain period. PS and Vair stand for the surface pressure and the total column of air density used in TROPOMI XCH_4 retrieval. RH is the relative humidity.

2.1 Estimate methane emission from TROPOMI

There are two additive corrections, the stripe correction and the albedo correction, on XCH_4 to remove biases caused by the satellite retrieval. The detailed method can be found in Part A and B of Supplementary Information (SI).

The continuity equation connecting the divergence (*D*), emission (*E*) and sink (*S*) for steady state is: *D* = *E* + *S [Beirle et al., 2019]*. As the lifetime of CH_4 is around 10 years, the sink term can be ignored, that is: *D* = *E*. The divergence *D* works on horizontal fluxes (*F*): $D = \nabla F$, where *F* stands for zonal (Fu) and meridional fluxes (Fv), which is the product of gridded vertical columns (*V*) and horizontal wind fields ($\vec{w}$). For each day *d*:

$$E_d = \nabla F_d = \nabla(V \cdot \vec{w}) \qquad (1)$$

Numerical derivatives for *D* are calculated as the second-order central difference in this study. We convert XCH_4 to mean mixing ratio in the PBL, XCH_4^{PBL} (denoted by X^{PBL}), to eliminate the effects of orography and transport in upper atmosphere. The column of methane in the PBL (V^{PBL}) for day *d* is derived by:

$$V_d^{PBL} = X_d^{PBL} \times A_d^{PBL} \qquad (2)$$

where A_d^{PBL} is the corresponding air density column in the PBL. Considering the relatively long lifetime of methane, *D* in the PBL actually contains the variations of its background and sources. As *D* is a linear operator, the daily D_d of the fluxes in the PBL can be written as:

$$D_d = D_d^B + D_d^S \qquad (3)$$

where D^B is the daily divergence of the background flux and D^S is the daily divergence caused by sources in PBL, respectively. Combining with Eq. (1) and (2), Eq. (3) can be written as:

$$D_d^S = \nabla((X_d^{PBL} - X_d^B) \times A_d^{PBL} \cdot \vec{w} \qquad (4)$$

where X_d^B is the background of X_d^{PBL}. It is hard to know the exact X_d^B, so we use the regional background (X_d^R) to approximate the X_d^B as will be stated in Sect. 2.2. Eq. (4) is then written as:

$$D_d^S = \nabla((X_d^{PBL} - X_d^R) \times A_d^{PBL} \cdot \vec{w}) \qquad (5)$$

Equation (5) is applied to the daily variations of CH_4, and the emission is estimated by averaging D_d^S over a time period:

$$E_d = \overline{D_d^S} = \overline{D_d - D_d^R} \qquad (6)$$

where D^R stands for the averaged divergence of the regional background. However, we found a significant correlation between $\overline{D^S}$ and $\overline{D^R}$ at some locations, which suggest that the derived emissions still contain part of the background. Strong spatial positive correlations R are typically found over areas with complicated terrain where the background is less homogenous.

To remove the remaining background, we apply a two-step posteriori correction. First of all, *E* is multiplied by the empirical "correlation correction factor" (1−R) to reduce the biases caused by regional background.

In addition, we find that areas with negative emissions *E* also have negative $\overline{D^R}$ and divergence of winds ($\overline{D^w}$), implying no significant sources. Thus, secondly, the grids with negative *E* are set to be zero in the final estimated emissions. The practice of this posteriori correction is presented in Sect. 3.

2.2 Calculating the regional enhancement of methane in PBL

The entire atmospheric column was divided into only 12 layers in the TROPOMI XCH_4 retrieval, which is too coarse to resolve the vertical distribution. To estimate the methane column above the PBL we use model results of EAC4 of CAMS (https://ads.atmosphere.copernicus.eu/cdsapp#!/dataset/cams-global-reanalysis-eac4?tab=overview). It is a global hourly reanalysis of atmospheric composition at a relative high spatial resolution, 0.75° horizontally and 60 layers vertically [*Inness et al.*, 2019], which contains no a priori CH_4 emissions. Thus, the spatial distribution of CH_4 is solely the result of transport and orography, which will be subtracted from TROPOMI observations to estimate the PBL concentration of CH_4.

The surface pressure of each pixel is adjusted by a high-resolution GMTED2010 Digital Elevation map [*Hasekamp et al.*, 2019], and the pressure at each layer of the EAC4 XCH_4 profile is recalculated accordingly. The number of dry air molecules in the entire column of the XCH_4 profile is scaled to the total number that is used for the retrieval of the pixel. We do not interpolate the averaging kernel (AK) to the layers of EAC4, because the AK is approximately equal to 1.0 at each layer [*Hasekamp et al.*, 2019]. In this way, we ensure the conservation of air mass for each pixel as well as the high-resolution vertical distributions of methane.

Considering the height of the planetary boundary layer (PBLH) from reanalysis or forecast dataset has large uncertainties and is occasionally too shallow, we fixed the PBLH at 500 meters above the ground. XCH_4^{PBL} is obtained by subtracting the column above 500 meters from the ground and dividing the remainder by the corresponding dry air density column. The XCH_4^{PBL} of each pixel is then used to build the daily gridded data at a resolution of 0.25 °. In this study, for each grid, daily regional background of XCH_4^{PBL} (XCH_4^{R}) is defined as the average of the lower 10 percentile of its surrounding ±5 grid cells (11×11=121 grid cells in total by taking the current grid cell as the center). The difference between XCH_4^{PBL} and XCH_4^{R} (Eq. (5)) is finally used to calculate the divergence with wind speeds. Therefore, the system biases between EAC4 and TROPOMI is implicitly removed by subtracting XCH_4^{R} from XCH_4^{PBL}.

The wind field halfway the PBLH close to the overpass time is obtained from the ECMWF. The divergence method works only when transport takes place, i.e. there is at least some wind. In addition, extremely high wind speeds are not favorable for the method that is based on the regional mass balance. Therefore, wind speeds are constrained between 1 m/s to 10 m/s in this study.

2.3 Using a GEOS-Chem simulation to test the method

In order to evaluate the feasibility of our method, the case of a model simulated XCH_4 is suitable because of known a priori emissions. In this study, we perform a 3-month simulation starting from 1 July 2012 by the GEOS-Chem 12.5.0 (http://geos-chem.org) nested model over North America at a resolution of 0.5° lat. × 0.625° lon. with 47 vertical layers extending to the mesosphere. The boundary conditions are provided by GEOS-Chem global simulation at 4° lat. × 5° lon. using posterior methane emissions and OH levels inversed from GOSAT satellite observations [*Lu et al.*, 2021], and therefore these boundary conditions are unbiased to GOSAT observations outside the domain. Both models are driven by MERRA-2 reanalysis meteorological fields from the NASA Global Modeling and Assimilation Office (GMAO) [*Gelaro et al.*, 2017]. The a priori natural emissions include wetlands, open fires, termites and seeps. The anthropogenic emissions are from EDGAR v4.3.2 , with fugitive fuel emissions (oil, gas, coal) overwritten by the *Scarpelli et al.* [2020] inventory, and further superseded by the gridded version of Inventory of U.S. Greenhouse Gas Emissions and Sinks from the Environmental Protection Agency (EPA GHGI) over the US [*Maasakkers et al.*, 2016]. More information on the model setup can be found in [*Lu et al.*, 2021]. Here we take the results at UTC 18:00, which is close to the overpass time of TROPOMI over the US. We apply our method to these simulations of XCH_4 in the PBL. The XCH_4^{PBL} is the mixing ratio of the column in PBL at the same time. The method to build regional background for each grid follows Sect. 2.2.

3 Results

3.1 Verification of the method using GEOS-Chem simulations

Figure 2(a-c) shows the spatial distribution of the 3-month average of a priori emissions used in GEOS-Chem simulation, the divergence of XCH_4 enhancement in PBL and the estimated emission. Although the horizontal resolution of the model is much coarser than TROPOMI observations, the sources have been identified (Fig. 2(b)-(c)), even for relatively small emissions less than 2.5 kg/km^2/h. For the mountainous and coastal areas that are more complex than typical flat land terrain, the performance of the divergence works fairly well. Some fake signals caused by orography (e.g., in Mexico, convergence over oceans near the coastal) are successfully removed by the posteriori "correlation correction". The influence from the remaining background is mostly found over the grid cells with R greater than 0.7.

We further quantitatively compare the estimated emissions with the a priori emission inventory. The grid cells with emissions > 0 in the a priori inventory have been selected as the reference. The scatter plots in Fig. 2(d) and (e) compare a priori emissions greater than zero and greater than 4 kg/km^2/h with their counterparts respectively. Our estimated emissions capture the spatial variability in a priori emissions throughoutthe full range of emissions ($R^2 = 0.63$). The Reduced Major Axis (RMA) regression show a slope of 0.87 and an intercept of -0.08, highly implying the capability of our method in retrieving model emissions using simulated columns. The biases are mainly related to the simplified regional background we used. The big sources (a priori emission greater than 4 kg/km^2/h) are much easier to capture by our method ($R^2 = 0.78$, $R = 0.88$). The final result shows the simple regional background removal is simplified but efficient.

We also test our method by using the enhancement in the troposphere instead of the PBL (Fig. S5). The estimated emissions show a much weaker correlation with a priori emissions, especially over the areas with complicated orography. The transport in the upper troposphere are intervening with the emission estimates. Therefore, using the enhancement of XCH_4 in the PBL is more suitable to identify and quantify the emissions.

3.2 CH_4 emissions over the US based on TROPOMI

Figure 3(a) presents the spatial distributions of TROPOMI yearly-averaged XCH_4 after destriping and SWIR surface albedo corrections over North America on a 0.25° grid in 2019. After converting XCH_4 to XCH_4^{PBL}, the spatial distribution of CH_4 becomes more continuous over mountains in Fig. 3(b). Despite the uncertainty from surface albedo corrections (see more detailed discussion in Part B of SI), enhancements of CH_4 are

found over Texas, California and Appalachia regions when comparing to the regional background (Fig. 3(c)).

Figures 3(d)-(e) show examples of the divergence of sources and of corresponding regional backgrounds in the PBL over the Texas area, one of the most prolific petroleum- and gas-producing regions in the U.S., and Fig. 3(f) shows their spatial correlation. The areas with negative values (convergence) in Fig. 3(d) are also negative in Fig. 3(e), demonstrating there are no significant sources. In addition, high positive spatial correlations mainly appear over the areas with complicated orography but few emissions. On the contrary, the areas with big sources have weak or negative spatial correlations between sources and regional backgrounds (Fig. 3(f)). Here we apply the "correlation correction" for grids with R greater than 0.0 to reduce the biases of the regional background we built.

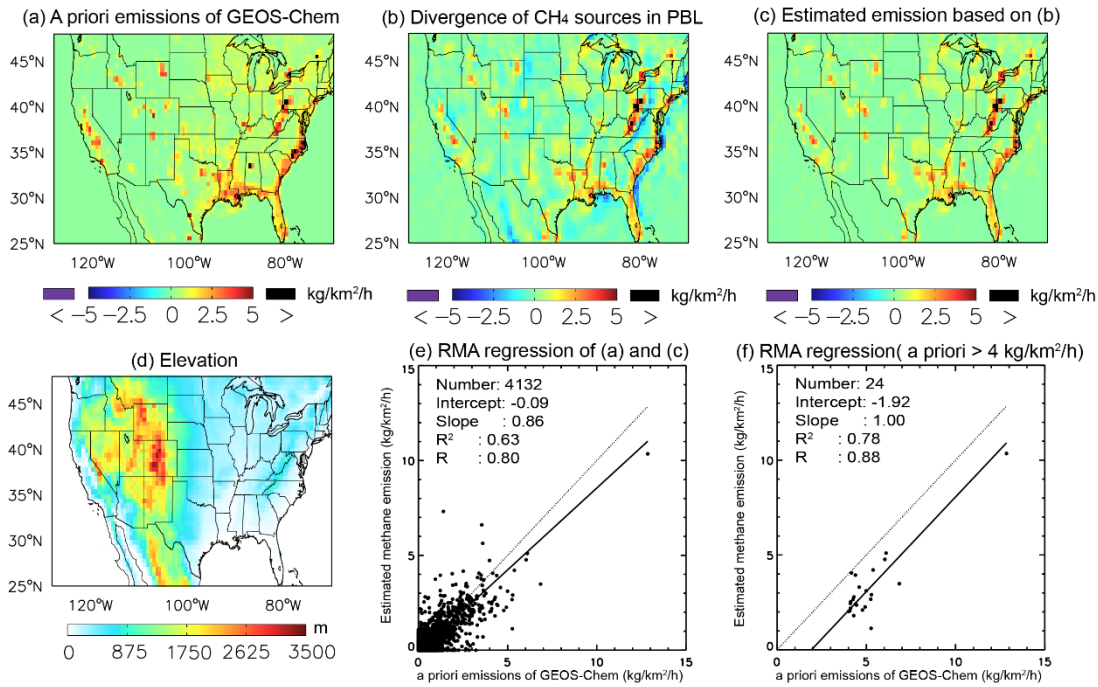

Figure 2. The spatial distributions of (a) the average of a priori CH_4 emissions used in GEOS-Chem simulation, (b) the divergence of CH_4 sources in PBL, and (c) corresponding estimated CH_4 emissions over June-August 2012 on a 0.625° lon. × 0.5° lat. grid. (d) The elevation map that is generated from GMTED2010 data set. (e) Scatter plots for emissions between a priori emissions higher than 0.0 kg/km^2/h and estimated CH_4 emissions. (f) As (e) but for a priori emissions that are higher than 4.0 kg/km^2/h. Each dot in (e) and (f) represents a grid cell.

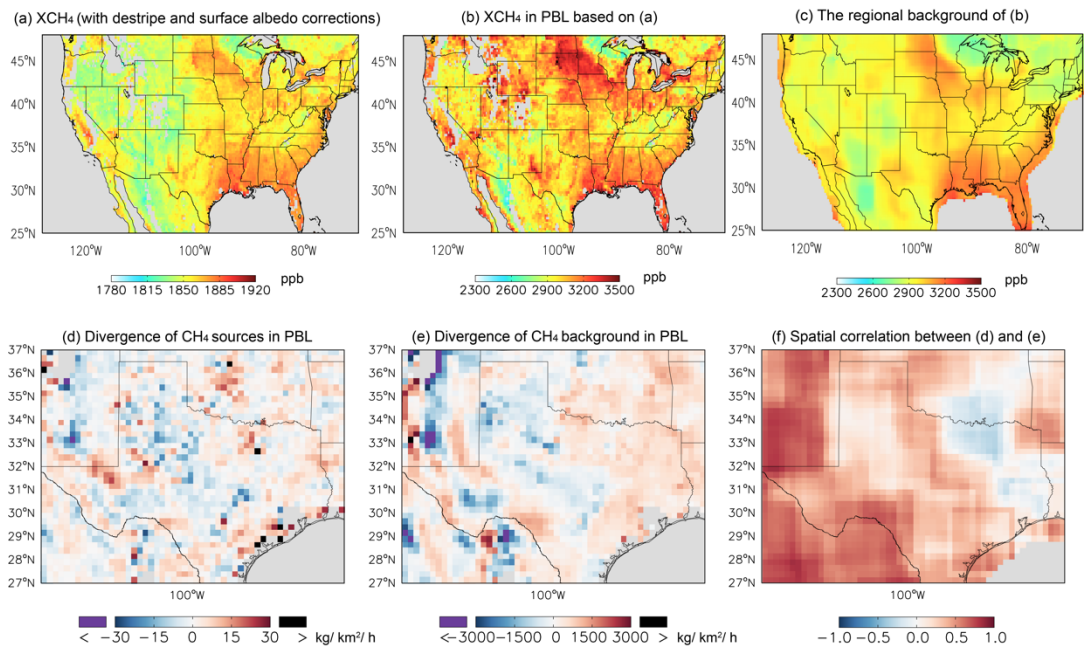

Figure 3. Spatial distributions of yearly averaged (a) XCH_4 with the stripe and surface albedo corrections, (b) the corresponding XCH_4 in PBL and (c) its regional background. The divergences of (d) CH_4 sources in PBL and (e) of the regional background in 2019. (f) The spatial correlation between (d) and (e). For each grid cell, the correlation is calculated in a domain of 11×11 grid cells, taking the grid cell as center.

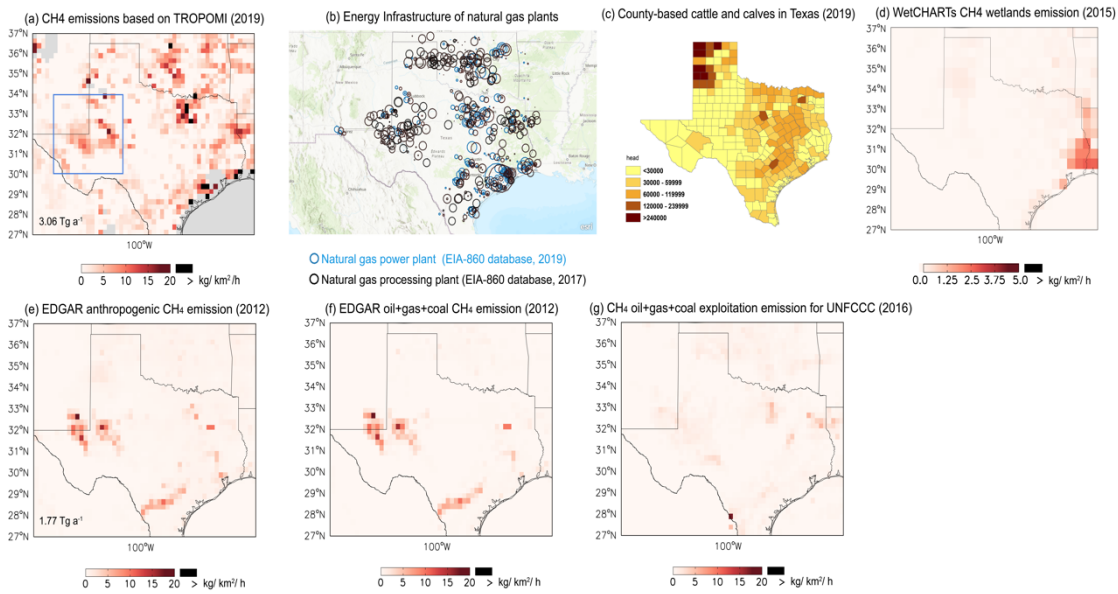

Figure 4. CH_4 emissions over the Texas area. (a) Our estimated emissions for 2019. (b) Natural gas power plants (blue circles) and processing plants (black circles) in Texas (available at: https://www.eia.gov/special/gulf_of_mexico/). The size of each circle represents the capacity of the plant. (c) County-based heads of cattle and calves in Texas in 2019 (available at: https://www.nass.usda.gov/Statistics_by_State/Texas/Publications/County_Estimates/ce_maps/ce_catt.php) (c) EDGAR v4.3.2 for the total anthropogenic emissions in 2012 (available at: https://edgar.jrc.ec.europa.eu/overview.php?v=432_GHG), (d) WeCHARTs wetland emissions for 2015 [*Bloom et al.*, 2017], (e) EDGAR v4.3.2 anthropogenic CH_4 total emissions for 2012. (f) EDGAR v4.3.2 CH_4 oil+gas+coal emissions in 2012, and (g) a global inventory of methane emissions from oil, gas, and coal exploitation that spatially allocates the national emissions reported to the UNFCCC for 2016 [*Scarpelli et al.*, 2020]. The area enclosed by the solid blue line is the Permian Basin (30°-34°N, 101°-105°W). The annual total emissions of CH_4 based on our estimates and EDGAR v4.3.2 over the Permian Basin are embedded in the left corner of (a) and (e).

Our method not only successfully identified the sources in abovementioned well-known oil/gas fields, but also shows the ability to capture the sources from other sectors such as livestock and wetlands. For example, the high CH_4 emissions north of the Permian Bas in Fig. 4(a) are very likely coming from a large number of cattle farms there (Fig 4(b)). Dairy farms or feed yards in this region are typically open lot, and sources of CH_4 are enteric emissions from cattle and emissions of wastewater lagoons. The emission rate of cattle is estimated to be on average 0.211 kg/head/day [*Todd et al.*, 2011]. These biogenic emissions do not exist in oil/gas/coal emissions in Fig. 4(f)-(g) but can be found as small contributions to EDGAR v4.3.2 total emissions (Fig. 4(e)).

TROPOMI CH_4 retrievals are not available over water, which inevitably leads to uncertainties and limited number of observations near coasts, lakes and bays. However, the natural gas power/processing plants onshore Texas near western Gulf of Mexico (Fig. 4(b)), which shows the energy infrastructures of U.S Energy Information Administration [*EIA*], are found near the locations of sources shown in Fig. 4(b). It implies that emissions relating to oil/gas productions in the coastal are caught by our divergence method.

We further quantify the annual average CH_4 emissions over the Permian Basin (enclosed by the solid blue boundary in Fig. 4(a)). Our estimated emissions in 2019 (see baseline settings in Table S1) is 3.06 Tg a^{-1}, which is 42% higher than EDGAR v4.3.2 total anthropogenic emissions in 2012 (1.77 Tg a^{-1}), which can be due to an increase in oil production between 2012 and 2019. *Zhang et al.* [2020] estimated the total emission as 2.9 ± 0.5 Tg a^{-1} based on the S5P operational TROPOMI CH_4 product [*Hasekamp et al.*, 2019; *Landgraf et al.*, 2019] from May 2018 to March 2019 by using inverse modeling with a priori emissions. The average annual emissions for the time period 2018/2019 based on the TROPOMI/WFMD v1.2 [*Schneising et al.*, 2019] product is reported as 3.18 ± 1.13 Tg a^{-1} by *Schneising et al.* [2020] using a mass balance method.

In addition to testing different surface albedo corrections (see Part B in SI), we designed several other sensitivity tests to discuss the uncertainties of our estimated emissions that are generated from assumptions on the PBLH, the regional background concentration and wind speeds. Table S1 shows the different results for each case and the baseline method, called REF, over the Texas area. The mean, median, maximum and minimum difference relative to REF in Texas are listed. The total emission of each case over the Permian Basin is also quantified (last column in Table S1). Figure S5-S7 are corresponding spatial distributions of estimated emissions and the difference with reference to the REF by using different assumptions of PBLH, the regional background and the wind speeds, respectively.

PBLHs varying from 300m to 1000m were tested. The influence of the PBLH on the spatial pattern and the total amount of final emissions are small, especially for the cases

below 1000m. We also changed the size of the background region from surrounding 3 grid cells to 7 grid cells (in each direction), leading to a bias of at most -0.19 Tg a^{-1} for the total emissions of the Permian Basin. As expected, the smaller size of the regional background (e.g. 3 grid cells) lead to a higher regional background over the areas with big sources. Thus, the estimated emissions are decreasing over the emissions clusters while the emissions around them often increase.

We tested various restrictions on the maximum and minimum wind speed (Figure S8). The influence of wind speed is more complicated. Unlike the tests of PBLH and regional background, different restrictions firstly affect the samplings of days. High wind speeds lead to large uncertainties over areas with complicated terrain. For example, large divergence values near the mountains close to the west of the Permian Basin, are not sufficiently removed with the "correlation correction" (Fig. S8 (a)). The smearing effect by high wind speeds lead to homogenous spatial distributions of XCH_4 in the PBL. The signals of sources are hard to be separated from the regional background. It also indicates that cases with high wind speeds are not handled well by our method, and are therefore excluded. In contrast, constraints on lowest wind speeds have smaller effects on final emissions (Fig. S8 (e)-(f)), because pollutants exhibit much stronger horizontal gradient in calm scenes. But the divergence method works only if transportation related to wind exists, so we set the minimum wind speed at 1m/s.

4 Conclusions

A new divergence method has been successfully developed and applied to estimate CH_4 emissions over Texas in North America based on observations of the TROPOMI instrument. The method works fairly well to detect sources of all strengths, proven by using a GEOS-Chem model simulation as an ideal case. Applied to real TROPOMI observations it clearly identifies signals from oil/gas clusters and other sources, such as livestock and wetlands. Further quantification of annual averaged CH_4 emissions over the Permian Basin area is consistent with recent previous studies. The different spatial distributions of emissions in different inventories (ranging from 2012-2019) imply strong temporal variations of emissions in this area. The divergence method we built benefits from TROPOMI's high spatial resolution and provides a way to quickly estimate CH_4 emission from satellite observation. The method does not need use any a priori information on location of strength of the emissions.

Through the sensitivity tests on the PBLH, the regional background and the wind speeds, the uncertainties of estimated emissions could be reduced by constraining their values. High wind speeds cause high uncertainties over areas with complicated terrain. In future work the uncertainties caused by the winds will be reduced when longer records of background concentrations, EAC4 dataset, are available. The higher spatial resolution of the estimated emissions is another aspect to be improved after the new S5P TROPOMI CH_4 dataset will be released.

Acknowledgments

Competing interests. The authors declare that they have no competing interests.

Author contributions. ML, RVA, and MVW designed the experiment. All GEOS-Chem simulations over the US were conducted by XL. ML performed all calculations. The codes for estimating methane emissions are mainly developed by ML and are supported by HE and PV. HK, JW, JS, and JD help to visualize the results. JL provided the script to download the TROPOMI methane L2 file. The wind fields are extracted by HE. YZ and HW help to access the GESO-FP meteorological dataset. All co-authors contributed to review the manuscript.

Data and materials availability:

S5P TROPOMI methane Level-2 dataset is available at: http://www.tropomi.eu/data-products/methane

EAC4 of CAMS, which used to be estimated the column above the PBL can be accessed at: https://ads.atmosphere.copernicus.eu/cdsapp#!/dataset/cams-global-reanalysis-eac4?tab=overview

Natural gas power plants and processing plants in Texas are available at: https://www.eia.gov/special/gulf_of_mexico/

County-based heads of cattle and calves in Texas in 2019 is available at: https://www.nass.usda.gov/Statistics_by_State/Texas/Publications/County_Estimates/ce_maps/ce_catt.php

EDGAR v4.3.2 for the total anthropogenic emissions in 2012 is available at: https://edgar.jrc.ec.europa.eu/overview.php?v=432_GHG

WeCHARTs wetland emission in 2015 can be found at: https://daac.ornl.gov/cgi-bin/dsviewer.pl?ds_id=1502

The GEOS-Chem simulation dataset will be upload to the Amazon Drive after this paper is accepted.

Reference

Beirle, S., C. Borger, S. Dörner, A. Li, Z. Hu, F. Liu, Y. Wang, and T. Wagner (2019), Pinpointing nitrogen oxide emissions from space, *Science Advances*, *5*(11), eaax9800.

Bloom, A. A., K. W. Bowman, M. Lee, A. J. Turner, R. Schroeder, J. R. Worden, R.

Weidner, K. C. McDonald, and D. J. Jacob (2017), A global wetland methane emissions and uncertainty dataset for atmospheric chemical transport models (WetCHARTs version 1.0), *Geosci. Model Dev.*, *10*(6), 2141-2156.

Buchwitz, M., et al. (2017), Global satellite observations of column-averaged carbon dioxide and methane: The GHG-CCI XCO2 and XCH4 CRDP3 data set, *Remote Sensing of Environment*, *203*, 276-295.

de Gouw, J. A., J. P. Veefkind, E. Roosenbrand, B. Dix, J. C. Lin, J. Landgraf, and P. F. Levelt (2020), Daily Satellite Observations of Methane from Oil and Gas Production Regions in the United States, *Scientific Reports*, *10*(1), 1379.

Dlugokencky, E. J., et al. (2009), Observational constraints on recent increases in the atmospheric CH4 burden, *Geophysical Research Letters*, *36*(18).

EIA (2021), Energy Infrastructure with Real-Time Storm Information, edited, U.S. Energy Information Administration, Washington, DC.

Gelaro, R., et al. (2017), The Modern-Era Retrospective Analysis for Research and Applications, Version 2 (MERRA-2), *Journal of Climate*, *30*(14), 5419-5454.

Hasekamp, O., A. Lorente, H. Hu, A. Butz, J. aan de Brugh, and J. Landgraf (2019), Algorithm Theoretical Baseline Document for Sentinel-5 Precursor Methane Retrieval(1.10).

Inness, A., et al. (2019), The CAMS reanalysis of atmospheric composition, *Atmos. Chem. Phys.*, *19*(6), 3515-3556.

IPCC (2013), Climate Change 2013: The Physical Science Basis. Contribution of Working Group I to the Fifth Assessment Report of the Intergovernmental Panel on Climate Change edited, Cambridge University Press, New York.

Landgraf, J., A. Butz, O. Hasekamp, H. Hu, and J. aan de Brugh (2019), Sentinel 5 L2 Prototype Processors, Algorithm Theoretical Baseline Document: Methane Retrieval, SRON-ESA-S5L2PP-ATBD-001-v3.1-20190517-CH4, edited, SRON Netherlands Institute for Space Research.

Liu, M. Y., et al. (2020), A new TROPOMI product for tropospheric NO2 columns over East Asia with explicit aerosol corrections, *Atmos. Meas. Tech.*, *13*(8), 4247-4259.

Lu, X., et al. (2021), Global methane budget and trend, 2010–2017: complementarity of inverse analyses using in situ (GLOBALVIEWplus CH4 ObsPack) and satellite

(GOSAT) observations, *Atmos. Chem. Phys.*, *21*(6), 4637-4657.

Lunt, M. F., P. I. Palmer, L. Feng, C. M. Taylor, H. Boesch, and R. J. Parker (2019), An increase in methane emissions from tropical Africa between 2010 and 2016 inferred from satellite data, *Atmos. Chem. Phys.*, *19*(23), 14721-14740.

Maasakkers, J. D., et al. (2019), Global distribution of methane emissions, emission trends, and OH concentrations and trends inferred from an inversion of GOSAT satellite data for 2010–2015, *Atmos. Chem. Phys.*, *19*(11), 7859-7881.

Maasakkers, J. D., et al. (2016), Gridded National Inventory of U.S. Methane Emissions, *Environmental Science & Technology*, *50*(23), 13123-13133.

Miller, S. M., A. M. Michalak, R. G. Detmers, O. P. Hasekamp, L. M. P. Bruhwiler, and S. Schwietzke (2019), China's coal mine methane regulations have not curbed growing emissions, *Nature Communications*, *10*(1), 303.

Pandey, S., et al. (2019), Satellite observations reveal extreme methane leakage from a natural gas well blowout, *Proceedings of the National Academy of Sciences*, *116*(52), 26376.

Rigby, M., et al. (2008), Renewed growth of atmospheric methane, *Geophysical Research Letters*, *35*(22).

Saunois, M., et al. (2016), The global methane budget 2000–2012, *Earth Syst. Sci. Data*, *8*(2), 697-751.

Saunois, M., et al. (2020), The Global Methane Budget 2000–2017, *Earth Syst. Sci. Data*, *12*(3), 1561-1623.

Scarpelli, T. R., D. J. Jacob, J. D. Maasakkers, M. P. Sulprizio, J. X. Sheng, K. Rose, L. Romeo, J. R. Worden, and G. Janssens-Maenhout (2020), A global gridded (0.1° × 0.1°) inventory of methane emissions from oil, gas, and coal exploitation based on national reports to the United Nations Framework Convention on Climate Change, *Earth Syst. Sci. Data*, *12*(1), 563-575.

Schneider, A., T. Borsdorff, J. aan de Brugh, F. Aemisegger, D. G. Feist, R. Kivi, F. Hase, M. Schneider, and J. Landgraf (2020), First data set of H2O/HDO columns from the Tropospheric Monitoring Instrument (TROPOMI), *Atmos. Meas. Tech.*, *13*(1), 85-100.

Schneising, O., M. Buchwitz, M. Reuter, S. Vanselow, H. Bovensmann, and J. P.

Burrows (2020), Remote sensing of methane leakage from natural gas and petroleum systems revisited, *Atmos. Chem. Phys.*, *20*(15), 9169-9182.

Schneising, O., et al. (2019), A scientific algorithm to simultaneously retrieve carbon monoxide and methane from TROPOMI onboard Sentinel-5 Precursor, *Atmos. Meas. Tech.*, *12*(12), 6771-6802.

Shindell, D., et al. (2012), Simultaneously Mitigating Near-Term Climate Change and Improving Human Health and Food Security, *Science*, *335*(6065), 183.

Todd, R. W., N. A. Cole, K. D. Casey, R. Hagevoort, and B. W. Auvermann (2011), Methane emissions from southern High Plains dairy wastewater lagoons in the summer, *Animal Feed Science and Technology*, *166-167*, 575-580.

Turner, A. J., C. Frankenberg, and E. A. Kort (2019), Interpreting contemporary trends in atmospheric methane, *Proceedings of the National Academy of Sciences*, *116*(8), 2805.

Veefkind, J. P., et al. (2012), TROPOMI on the ESA Sentinel-5 Precursor: A GMES mission for global observations of the atmospheric composition for climate, air quality and ozone layer applications, *Remote Sensing of Environment*, *120*, 70-83.

Zhang, Y., et al. (2020), Quantifying methane emissions from the largest oil-producing basin in the United States from space, *Science Advances*, *6*(17), eaaz5120.

Geophysical Research Letters

Supporting Information for

A new divergence method to quantify methane emissions using observations of Sentinel-5P TROPOMI

Mengyao Liu[1]*, Ronald Van der A[1,2], Michiel Van Weele[1], Henk Eskes[1], Xiao Lu[3], Pepijn Veefkind[1,4], Jos de Laat[1], Hao Kong[5], Jingxu Wang[6], Jiyunting Sun[1], Jieying Ding[1], Yuanhong Zhao[6], Hongjian Weng[5]

[1] KNMI, Royal Netherlands Meteorological Institute, De Bilt, the Netherlands

[2] Nanjing University of Information Science & Technology (NUIST), Nanjing, China

[3] School of Engineering and Applied Sciences, Harvard University, Cambridge, MA 02138, USA

[4] Delft University of Technology, Delft, The Netherlands

[5] Department of Atmospheric and Oceanic Sciences, School of Physics, Peking University, Beijing, China

[6] College of Oceanic and Atmospheric Sciences, Ocean University of China, Qingdao, China

* Correspondence to: Mengyao Liu (mengyao.liu@knmi.nl)

This PDF file includes 15 pages containing

1. Part A: The stripe correction on XCH_4
2. Part B: Influence of surface albedo corrections on estimated CH_4 emissions
3. Figures S1 to S8
4. Table S1
5. SI references

Part A. The stripe correction on XCH_4

We apply the stripe correction on XCH_4 to remove across-track biases between the individual viewing angles of the satellite. The stripe correction is determined from Level 2 files by first applying a high-pass median filter in the across-track direction and next a high-pass median filter in the time direction (Borsdorff, personal communication 2020). The Level 2 files provide the data in two dimensions as scan lines (temporal direction) and ground pixels (across satellite track and approximately west-east). The first step for creating the stripe correction is performed per orbit. First a smoothed XCH_4 image is computed using a median filter in the across track direction, using the XCH_4 with qa_value > 0.5 for each ground pixel and its four eastern and western neighbors. At the eastern and western edge of the swath this number is less, but at least 4 neighboring pixels are taken into account. In this step, online scans with at least 20% valid data are taken into account. The across track striping pattern of the orbit is computed by subtracting the smoothed image from the XCH_4 data and subsequently taking the median in the temporal direction.

After computing the stripe pattern for all orbits, a smoothing between the orbits is performed by applying a median of the orbit and its 50 previous and 50 next orbits (note that 100 orbits cover approximately one week of data). Finally, a linear interpolation is performed in temporal direction to compute the striping correction for all orbits, including those for which too little data was available to compute the stripe pattern.

As shown in Figure S1, the corrections depend on the TROPOMI ground pixel index and orbit number. The changes of yearly averaged XCH_4 in 2019 before and after destriping

are within ±5 ppb (mean: −0.08 ppb) on a 0.25° grid. Figure S1 shows the difference with time before and after the stripe correction. For most ground pixels, the differences are within 10 ppb.

Part B. Influence of surface albedo corrections on estimated emissions

The current official TROPOMI bias-corrected XCH_4 product (XCH_4^{S5P}) is derived from a second order fit to the ratio of TROPOMI and GOSAT CH_4 as a function of SWIR albedo [*Hasekamp et al.*, 2019; *Lorente et al.*, 2021]. It is defined as:

$$XCH_4^{S5P} = XCH_4\,(c1 + c2 \cdot A + c3 \cdot A2) \qquad \text{(S1)}$$

where A is the surface albedo retrieved at the SWIR spectral range and c1 (=1.0173), c2 (=−0.1538), c3 (=−0.2036) are the correction parameters derived from a second order fit of the ratio of TROPOMI and GOSAT CH_4 as a function of albedo [*Hasekamp et al.*, 2019]. Although this posteriori correction reduces the general biases to ground-based TCCON observation, XCH_4^{S5P} is still likely to underestimate over the areas with low albedos and overestimate over very bright surface. These systematic biases can be seen clearly over Northern Africa in Fig S2, which covers a wide range of realistic surface albedos. The positive corrections given by Eq. (S1) for the areas with high albedos (>0.5) lead to high XCH_4^{S5P} comparing to uncorrected XCH_4 (Fig S2 (c)). Thus， the spatial pattern of XCH_4^{S5P} (Fig. S2 (b)) are quite similar to the SWIR surface albedo (Fig. S2 (d)). These biases of XCH_4^{S5P}, caused by the dependence on GOSAT observations and the lack of ground-based observations, have been also found by *Lorente et al.* [2021]. The new fitting function for the coming version becomes independent of GOSAT observations and monotonous (See Figure 4 in *Lorente et al.* [2021]).

To avoid the abovementioned biases caused by surface albedos, in this study, a piecewise linear fit to XCH_4 as a function of the corresponding SWIR surface albedo are designed to give a positive correction for low-albedo areas (< 0.1) and a negative correction for high-albedo areas (≥ 0.1). The junction point, where the albedo is equal to 0.1, of the piecewise linear fit functions is obtained from *Hasekamp et al.* [2019]. The advantage of the linear fitting is that the coefficient can be directly treated as correction factor (CF).

Therefore, the corrected TROPOMI XCH_4 (XCH_4^{CORR}) is $XCH_4 \cdot (1 + CF)$. CF is obtained as follows:

$$CF = CF_1 \cdot (0.1 - A) \qquad (A < 0.1) \qquad (S2)$$

$$CF = CF_2 \cdot A \qquad (A \geq 0.1) \qquad (S3)$$

where CF_1 is the positive-correction coefficient (= 671.0), and CF_2 is the negative-correction coefficient (= −63.5) derived from the two-segment linear fitting.

The fitting is based on the gridded yearly average of TROPOMI XCH_4 and corresponding SWIR surface albedo in 2019 over the US (the domain is showed in Fig. 2) on a 0.25° grid (the same spatial resolution as the later divergence calculation and the emission estimation). Only XCH_4 retrievals lower than 3000 ppb and with an elevation below 500 m are selected for the fitting. We use gridded data instead of observation pixels to avoid issues with seasonal variations and over-sampling.

Figure S3(a)-(b) are the spatial distributions of TROPOMI yearly-averaged XCH_4 after destriping and SWIR surface albedo corrections over the North America on a 0.25° grid in 2019. Some strong enhancements caused by landforms (e.g., rocks and deserts in Utah and Arizona; alluvial accumulation around Mississippi Delta) are clearly seen from Fig. 3(a). Figure 3(d) gives a more reasonable spatial pattern over North America. The overestimated XCH_4 due to the bare ground in western U.S. decrease while the concentration over the east coast increase after corrections (Fig. S3(d)). After converting XCH_4 to XCH_4^{PBL}, the spatial distribution of CH_4 becomes more continuous over mountains in Fig. S3(e). Despite the uncertainty from surface albedo corrections, enhancement of CH_4 are found over Texas, California and Appalachia regions when comparing to the regional background (Fig. S3(f)).

The third row presents spatial distributions of XCH_4 with the surface albedo corrections of the official S5P operational product (XCH_4^{S5P}). The overestimated XCH_4 due to the bare ground (i.e. high albedo) in western U.S. decrease after both corrections (Fig. S3 (d) and (g)). Relatively big differences in the two corrections are found over the east coast of the U.S., where our results are about ~15 ppb higher than XCH_4^{S5P} over the areas with dark surfaces (albedo < 0.1). The enhancements caused by wetlands over here are much

clearer in our corrections. The underestimation of XCH_4^{S5P} has also been improved in Lorente et al, [2021].

Figure S3 further quantified the difference caused by two different surface albedo corrections over Texas. In general, the locations of big sources are caught in both Fig. S4 (a) and (b). Big differences of estimated emissions appear over Mexico and the east of Texas. The big sources near the border of Lousiana and Texas in Fig. S4(b) seem to be biases in XCH_4^{S5P}.

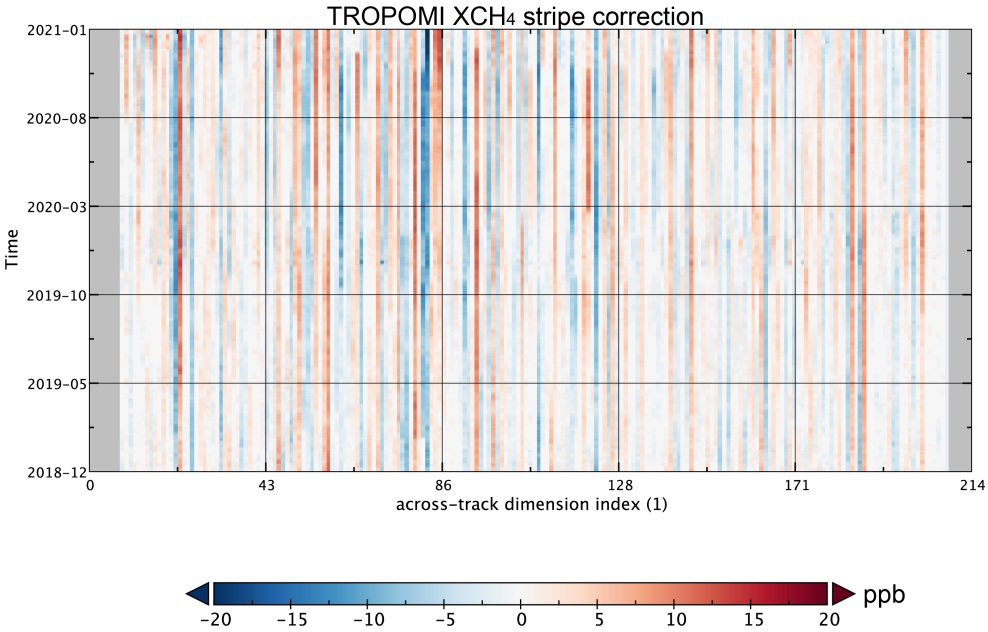

Figure S1. The difference over time before and after the stripe correction.

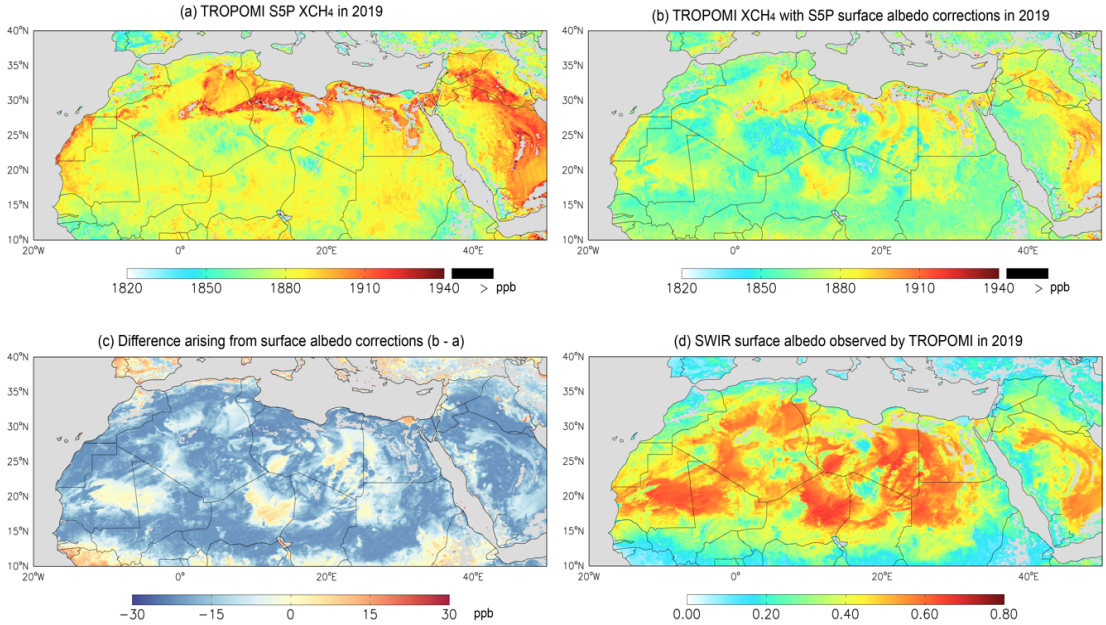

Figure S2. The spatial distributions of yearly averaged (a) XCH_4, (b) XCH_4^{S5P} and (c) their difference in 2019 on a 0.25° grid. (d) The TROPOMI observed SWIR surface albedos that is used to correct XCH_4.

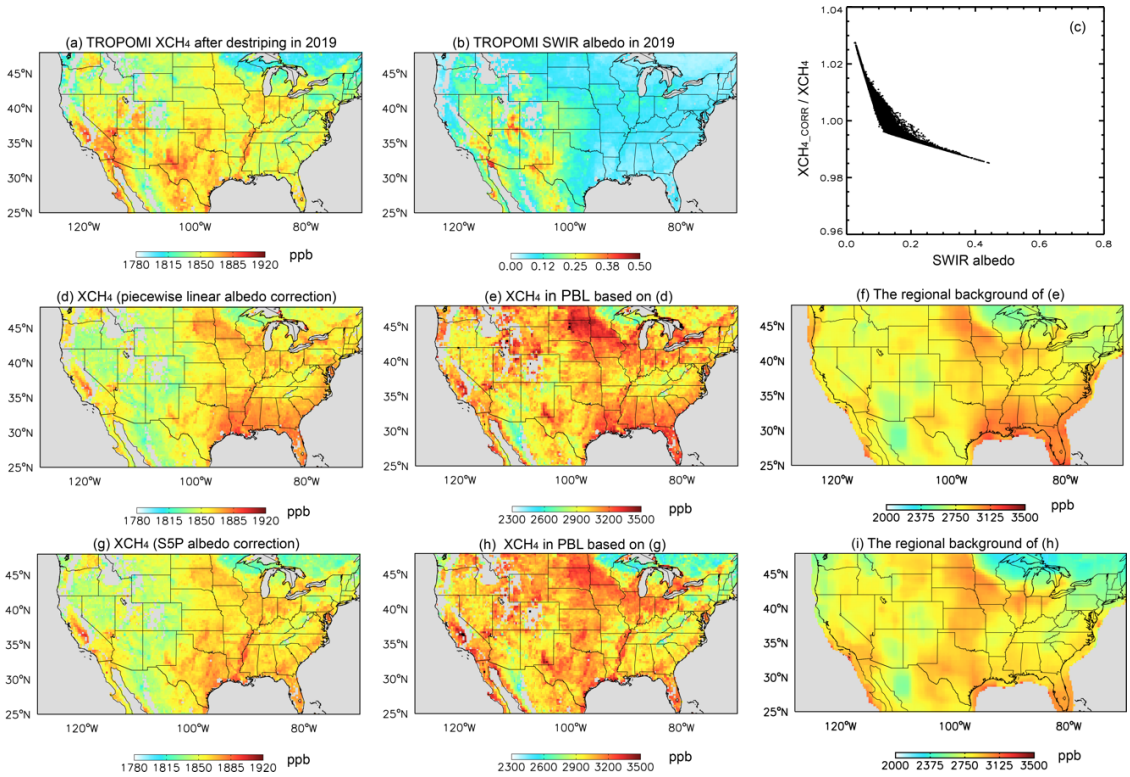

Figure S3. Yearly averages of (a) TROPOMI XCH_4 after destriping and (b) TROPOMI SWIR surface albedo in 2019 on a 0.25° grid. (c) The scatter plots of the ratios of XCH_{4_CORR}/XCH_4 and SWIR surface albedos. Each dot represents a grid cell in (a) and (b). Yearly averages of (d) XCH_4 with segment linear surface albedo corrections, (e) the corresponding XCH_4 in PBL and (f) its regional background. (g)-(i) are similar to (d)-(f) but for XCH_4 with S5P surface albedo correction.

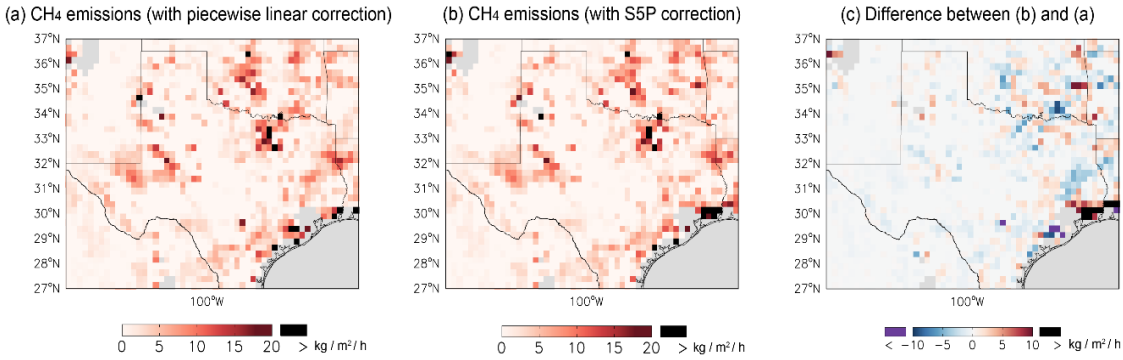

Figure S4. The estimated CH_4 emissions based on (a) XCH_4^{CORR}, (b) XCH_4^{S5P} and (c) their difference in 2019 on a 0.25° grid.

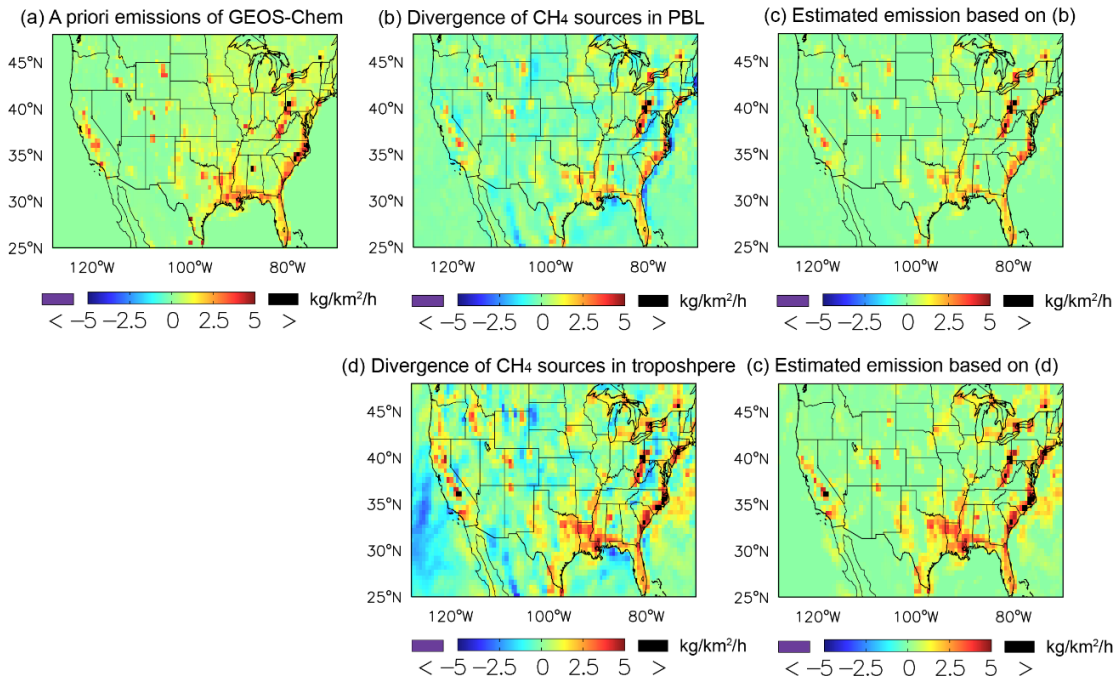

Figure S5. The spatial distributions of (a) the average of a priori CH_4 emissions used in GEOS-Chem simulation, (b) the divergence of CH_4 sources in the PBL, and (c) corresponding estimated CH_4 emissions over July-September 2012 on a 0.625° lon. × 0.5° lat. grid. (d)-(e) are similar to (b)-(c) but for the results using XCH_4 in the troposphere.

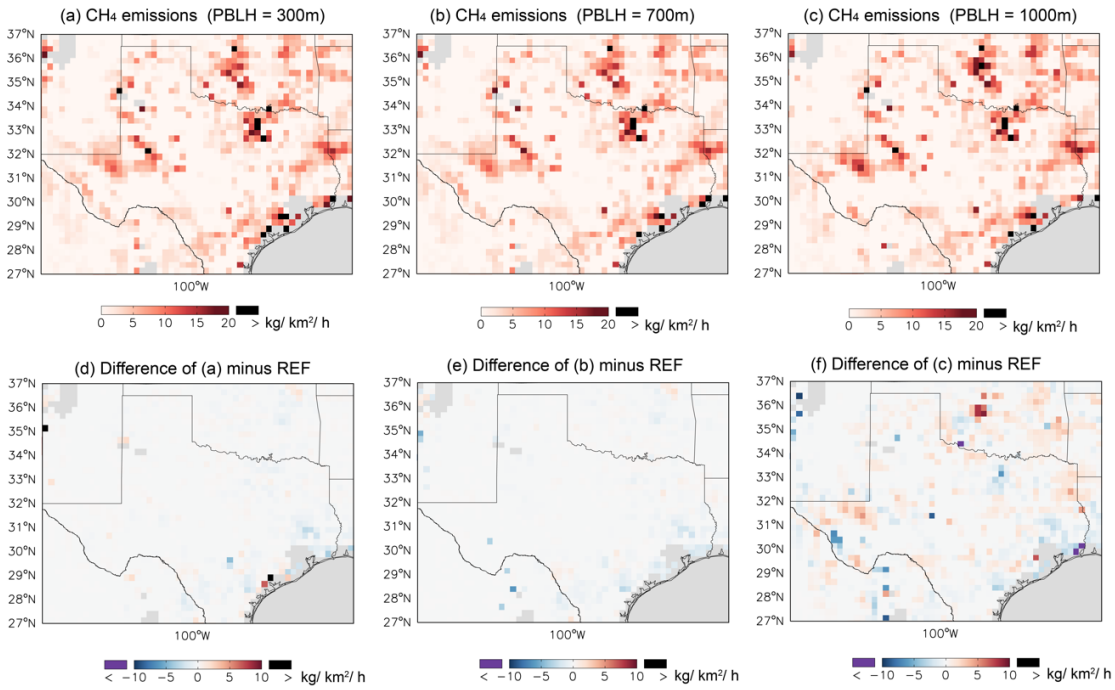

Figure S6. Results of different assumptions on PBLH. (a)-(c) are CH_4 emissions estimated with (a) PBLH = 300 m, (b) PBLH = 700 m, (c) PBLH = 1000 m and. (d)-(f) are corresponding differences of (a)-(c) minus REF.

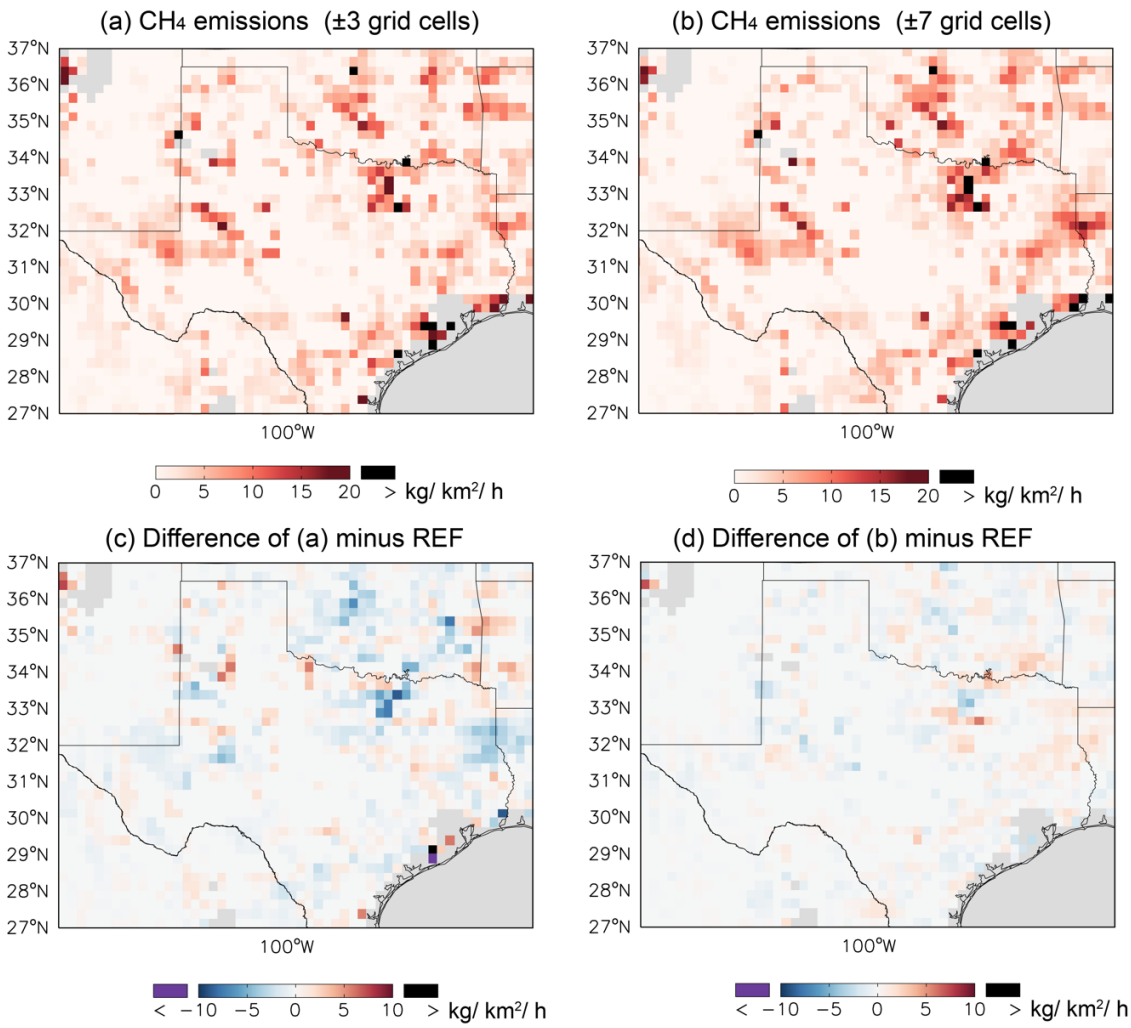

Figure S7. Results of different assumptions on the size of the background region from (a) surrounding 3 grid cells to (b) 7 grid cells (in each direction). (c)-(d) are corresponding differences of (a)-(b) minus REF.

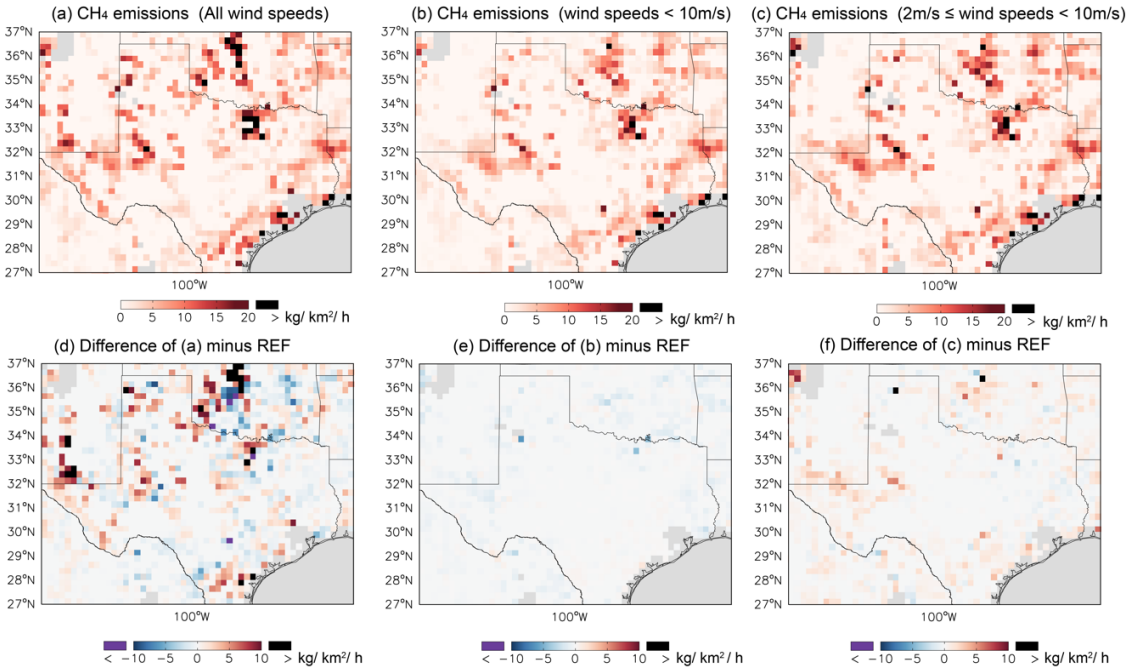

Figure S8. Results of different assumptions on the constraints of wind speeds (V). (a)-(c) are CH_4 emissions estimated with (a) all V, (b) V < 10 m/s, (c) 2 m/s < V < 10 m/s. (d)-(f) are corresponding differences of (a)-(c) minus REF.

Table S1. Results of sensitivity studies.

REF: 1 < V < 10 m/s; PBLH = 500m; Background: ±5 grid cells; 3.06 Tg a^{-1}

Difference with reference to REF[1]	Mean ($kg/km^2/h$)	Medium ($kg/km^2/h$)	Min ($kg/km^2/h$)	Max ($kg/km^2/h$)	Total emission of Permian Basin[4] (Tg a^{-1})
Wind speeds (m/s)					
V < 10	−0.2	−0.1	−10.4	1.44	2.82
2 < V < 10	0.5	0.3	−4.7	14.7	3.78
All	0.1	0.0	−29.8	30.5	3.60
PBLH (m)[2]					
300	−0.05	0.0	−4.5	6.8	3.06
700	−0.1	−0.02	−6.2	1.9	3.04
1000	0.07	0.1	−22.4	9.2	3.37
Background[3]					
±3 grid cells	−0.3	−0.2	−12.0	11.2	2.87
±7 grid cells	0.0	0.0	−4.4	7.1	3.00

[1] The value of mean, medium, minimum and maximum is the difference with the reference (REF) in the domain (27°-37°N, 106.5°-93°W) of Fig. 4.
[2] The PBLH is the height above the ground.
[3] The tested parameter is the number of surrounding grid cells that are used to generate the background.
[4] The domain of the Permian Basin is 30°-34°N, 101°-105°W, shown in Fig. 4(a)

References:

Hasekamp, O., A. Lorente, H. Hu, A. Butz, J. aan de Brugh, and J. Landgraf (2019), Algorithm Theoretical Baseline Document for Sentinel-5 Precursor Methane Retrieval(1.10).

Lorente, A., et al. (2021), Methane retrieved from TROPOMI: improvement of the data product and validation of the first 2 years of measurements, *Atmos. Meas. Tech.*, *14*(1), 665-684.